Check for updates

AGU100 ADVANCING EARTH AND SPACE SCIENCE

JAMES | Journal of Advances in Modeling Earth Systems

RESEARCH ARTICLE
10.1029/2020MS002056

Key Points:
- The ascending area narrows as the heating there increases relative to the cooling in the sinking air
- The circulation weakens with warming because radiative cooling increases more slowly than stability
- Enhanced vertical moisture gradients and stratiform heating support decreased ascent area

Correspondence to:
A. M. Jenney,
Andrea.Jenney@colostate.edu

Citation:
Jenney, A. M., Randall, D. A., & Branson, M. (2020). Understanding the response of tropical ascent to warming using an energy balance framework. *Journal of Advances in Modeling Earth Systems*, *12*, e2020MS002056. https://doi.org/10.1029/2020MS002056

Received 11 JAN 2020
Accepted 11 MAY 2020
Accepted article online 16 MAY 2020

This article was prematurely published without the authors' corrections. Corrections were made on 18 June 2020, to incorporate the authors' changes.

©2020. The Authors.
This is an open access article under the terms of the Creative Commons Attribution License, which permits use, distribution and reproduction in any medium, provided the original work is properly cited.

Understanding the Response of Tropical Ascent to Warming Using an Energy Balance Framework

A. M. Jenney[1], D. A. Randall[1], and M. D. Branson[1]

[1]Department of Atmospheric Science, Colorado State University, Fort Collins, CO, USA

Abstract Previous work has established that warming is associated with an increase in dry static stability, a weakening of the tropical circulation, and a decrease in the convective mass flux. Using a set of idealized simulations with specified surface warming and superparameterized convection, we find support for these previous conclusions. We use an energy and mass balance framework to develop a simple diagnostic that links the fractional area covered by the region of upward motion to the strength of the mean circulation. We demonstrate that the diagnostic works well for our idealized simulations and use it to understand how changes in tropical ascent area and the strength of the mean circulation relate to changes in heating in the ascending and descending regions. We show that the decrease in the strength of the mean circulation can be explained by the relatively slow rate at which atmospheric radiative cooling intensifies with warming. In our simulations, decreases in tropical ascent area are balanced by increases in nonradiative heating in convective regions. Consistent with previous work, we find a warming-induced decrease in the mean convective mass flux. However, when we condition by the sign of the mean vertical motion, the warming-induced changes in the convective mass flux are nonmonotonic and opposite between the ascending and descending regions.

Plain Language Summary The circulation of the atmosphere is expected to weaken in a future warmer climate. Despite an expected increase in precipitation, studies show that the average strength of stormy updrafts (as measured by the average speed of the updrafts multiplied by their area) will also decrease. We use simulations with realistic representations of storms to test these ideas and derive an equation that may help us better understand how the strength of the circulation is linked to changes in its energy balance.

1. Introduction

The mean tropical circulation is closely coupled to convection. Mean rising motion occurs in relatively warm and moist regions, in association with active deep cumulus convection. This upward motion is balanced by slow, radiatively driven subsidence that occurs in drier regions, where cumulus convection is suppressed.

For reasons discussed below, both the tropical mean circulation and the low-level convective mass flux are expected to weaken in a future, warmer climate (Betts & Ridgway, 1989; Chou & Chen, 2010; Held & Soden, 2006; Knutson & Manabe, 1995; Schneider et al., 2010; Seager et al., 2010; Vecchi & Soden, 2007). The mean circulation is the net vertical mass flux over an area large enough to contain many convective clouds and is the sum of the mass fluxes of narrow convective updrafts and downdrafts and the vertical mass flux of their broad, quiescent environment.

Betts and Ridgway (1989) were the first to suggest that the tropical mean circulation would weaken with warming. Using a simple model of the tropical boundary layer, they found that the subsidence required for thermodynamic equilibrium weakened as sea surface temperatures (SSTs) warmed. Their conclusions were supported by the results of Knutson and Manabe (1995), who found that a global circulation model (GCM) simulated a weakening of the mean circulation with warming.

The response of the mean circulation can be understood in terms of the area-averaged dry static energy budget:

$$\frac{\partial \bar{s}}{\partial t} = -\overline{\mathbf{v}_h} \cdot \nabla \bar{s} - \bar{w}\frac{\partial \bar{s}}{\partial z} + \overline{Q_R} + \overline{Q_c}. \quad (1)$$

Here s is dry static energy, $\mathbf{v}_h$ is the horizontal wind vector, w is the vertical velocity, Q_R is the radiative heating rate, Q_c is the nonradiative heating rate due to cloud processes and turbulence, and an overbar represents an area average. In a dry statically stable atmosphere, $\partial s/\partial z > 0$. In the tropics, and for time scales longer than a few hours or a day at most, Equation 1 can be approximated by the "weak temperature gradient" (WTG) balance (Charney, 1963; Sobel & Bretherton, 2000; Sobel et al., 2001):

$$\bar{w}\frac{\partial \bar{s}}{\partial z} = \overline{Q_R} + \overline{Q_c}. \tag{2}$$

In the absence of nonradiative heating (i.e., for $\overline{Q_c} = 0$), 2 reduces to a balance between radiative cooling ($\overline{Q_R} < 0$) and the warming due to downward advection of dry static energy (i.e., $\bar{w} < 0$). Many studies have shown that in a warming climate the tropical static stability increases, roughly following the more stable moist adiabat associated with warmer surface temperatures. The fractional change in the static stability is larger than the fractional change in the radiative cooling rate, so that 2 implies slower subsidence in nonconvective regions.

Held and Soden (2006) proposed that the globally averaged convective mass flux will also decrease with warming. This is the vertical mass flux associated with convective updrafts (and downdrafts). The mass flux associated with convective updrafts is given by

$$M_u = \rho \sigma_u w_u, \tag{3}$$

where ρ is the density of the air, σ_u is the fractional area covered by the convective updrafts, and w_u is the vertical velocity of the convective updrafts. A similar formula gives M_d, the mass flux associated with convective downdrafts. Held and Soden (2006) expressed the globally averaged moisture budget in the form

$$P = \left(M_u\right)_B q_B. \tag{4}$$

Here P is the surface precipitation rate, $\left(M_u\right)_B$ is the lower tropospheric value of M_u, and q_B is the lower tropospheric water vapor mixing ratio. Changes in the globally averaged latent heat release associated with precipitation are mainly balanced by changes in atmospheric radiative cooling (e.g., Riehl & Malkus, 1958). Allen and Ingram (2002) argued that, as the climate warms, the fractional increase in P will be much smaller than the fractional change of q_B, which increases following Clausius-Clapeyron scaling. Based on this idea, Held and Soden (2006) concluded from 4 that M_B must decrease with warming. Vecchi and Soden (2007) provided support for this conclusion, based on an analysis of results from a suite of GCMs.

In summary, energy balance suggests that the subsidence *velocity* will weaken with warming, and moisture balance suggests that the lower tropospheric convective mass flux will also weaken with warming. Caution is needed before concluding that these changes imply a weakening of the circulation as measured by the total upward (or downward) mass flux. For example, slower subsidence over a broader region can give the same downward mass flux. In fact, an expansion of subsiding regions and a contraction of ascending regions have been observed in the historical record and produced in simulations of warming (e.g., Byrne & Schneider, 2016a, 2016b; Byrne et al., 2016b; Hu & Fu, 2007; Lau & Kim, 2015; Lu et al., 2007; Su et al., 2017, 2019; Wodzicki & Rapp, 2016).

Additionally, although the mass flux of the large-scale mean circulation is expected to be upward when and where the mass flux of deep convective clouds is upward, there are important differences between the two (Arakawa & Schubert, 1974; Betts, 1998). The mean mass flux includes partially canceling contributions from much stronger local convective updrafts and downdrafts, as well as vertical motions in the broad environment between the convective drafts. For example, Schneider et al. (2010) estimated that the rate at which mass ascends in convective updrafts may be up to five times larger than the mean upward motion, simply because of compensating downward motions in the same region. A more detailed discussion is given later.

For the reasons outlined above, the current paradigm of warming-induced weakening of both the tropical mean circulation and the tropical convective mass flux needs further study, in part because a weakening of the tropical circulation and/or convective mass flux may contribute to a weakening of teleconnections between the topics and middle latitudes (Bui & Maloney, 2018, 2019; Wolding et al., 2017). In this paper we use idealized simulations of global radiative-convective equilibrium (RCE) to investigate warming-induced changes to the mean circulation and convective mass flux.

2. Methods

2.1. Model

Simulations of the future climate are sensitive to convective parameterizations (e.g., Maher et al., 2018). Models participating in the Coupled Model Intercomparison Project Phase 5 vary widely in their projections of the strength of the mean tropical circulation (Byrne et al., 2018), mostly due to differences in convective parameterizations between the models (Schiro et al., 2019). The resulting uncertainties can be avoided by using global convection-resolving models (CRMs; e.g., Stevens et al., 2019), but for now the high computational cost of such models limits their use in global climate change simulations. Superparameterization offers an intermediate option, in which the conventional parameterizations of cloud and boundary layer processes are replaced by a simplified CRM embedded within each GCM grid cell (Grabowski, 2001; Khairoutdinov & Randall, 2001; Khairoutdinov et al., 2005; Randall et al., 2003). The CRM explicitly simulates the cloud-scale dynamics by solving the equation of motion. Cloud microphysics, radiative transfer, and turbulent mixing are parameterized on the CRM's fine grid. Despite the two-dimensionality of the embedded CRMs, which is needed to reduce the high computational cost of simulations, superparameterization enables more realistic simulations of a number of convectively coupled global processes (summarized byRandall et al., 2016). Key for the present study is that superparameterization makes it possible to directly diagnose changes in the convective mass flux and heating associated with cloud systems that are explicitly simulated by the CRM.

We will present results from a superparameterized (SP) version of the Community Atmosphere Model 4 (CAM4), using the finite-volume dynamical core and a 0.9° × 1.25° horizontal grid. Each GCM grid column hosts an embedded two-dimensional CRM, which has a horizontal grid spacing of 4 km with 32 columns. The CRMs share the bottom 24 of CAM4's 26 layers. Microphysics are computed by the CRM using a single-moment microphysics scheme, described in detail by Khairoutdinov and Randall (2003). For more details on SPCAM4 see Kooperman et al. (2016).

Following the experimental design of the RCE model intercomparison project (RCEMIP Wing et al., 2018), we simulated RCE using uniform solar insolation and uniform SSTs on a nonrotating planet. Using SSTs of 295, 300, and 305 K, the model was run for three simulated years. Our results are based on analysis of hourly and daily mean output for a 15-day extension at the end of Year 3. Data were saved on the native CAM4 0.9° × 1.25° horizontal grid, and for 26 hybrid-sigma model levels, with hybrid sigma vertical coordinate σ_h.

2.2. Diagnostics

For both the RCE and Earth simulations, we make use of a diagnostic quantity computed by the CRM and saved on the GCM grid. This is the nonradiative temperature tendency due to the embedded CRM (model variable name "SPDT"), horizontally averaged over the CRM's grid.

The model also provides convective mass flux diagnostics, which are computed using vertical velocities on the CRM's grid. The mass fluxes are computed on each CRM time step then time averaged for output at a specified interval. Following 3, the convective mass flux is the sum of the air density times the vertical velocity times the fractional area over CRM grid cells for which the average of the vertical velocities at the model level top and bottom is greater than (for updrafts) or less than (for downdrafts) a specified vertical velocity threshold. CRM cells with weaker vertical velocities do not contribute to the average. The specified threshold vertical velocity is used to distinguish convection from nonconvective processes, such as turbulence and gravity waves.

The threshold is of course somewhat arbitrary. To explore the sensitivity to the threshold, and also to obtain some information about the range of convective intensity, we computed convective mass fluxes using hourly vertical velocities in the same way as described above, but with three different vertical-velocity thresholds (0.5, 1, and 2 m s^{-1}). A test comparing the global mean convective mass fluxes computed using hourly versus instantaneous vertical velocities, both using the 2 m s^{-1} threshold, showed good agreement. In the plots shown later, we use the lowest threshold, 0.5 m s^{-1}, to diagnose the total convective mass flux. We categorize mass fluxes between 0.5 and 1 m s^{-1} as "weak" convection, between 1 and 2 m s^{-1} as "moderate" convection, and greater than 2 m s^{-1} as "intense" convection.

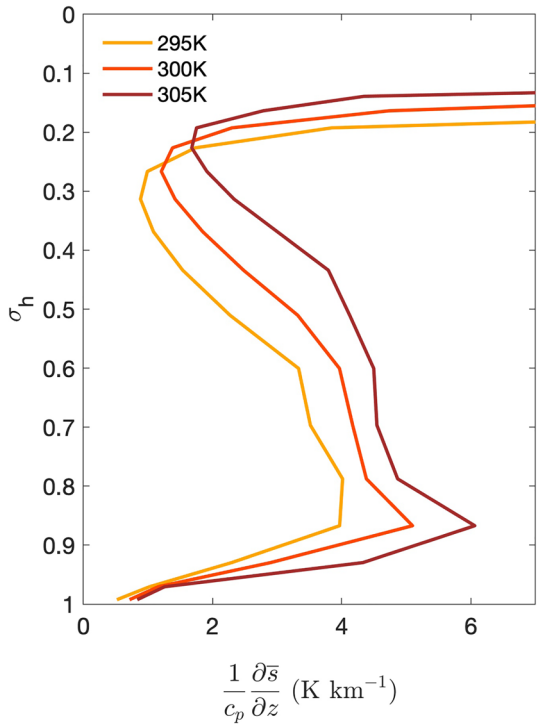

Figure 1. Mean static stability profiles for simulations. The vertical axis is the hybrid-sigma vertical coordinate, σ_h. We have divided by c_p, the specific heat of air at constant pressure, so the units are K km^{-1}.

3. Results

3.1. Mean Circulation

The global mean precipitation rate increases from 2.6 mm day^{-1} in the 295 K RCE simulation to 3.2 mm day^{-1} (a 4% K^{-1} increase) and 3.8 mm day^{-1} (3.5% K^{-1}) in the 300 K and 305 simulations, respectively. As expected for a boundary layer that is warming but maintaining a roughly constant relative humidity, the simulated increase in the water vapor mixing ratio of the lowest model level is about 6.8% K^{-1}.

Figure 1 shows the domain mean dry static stability profiles for these simulations. The dry static stability increases with warming, particularly at upper levels, as expected for a nearly moist-adiabatic lapse rate adjusting to warmer surface temperatures.

As discussed earlier, a weakening of the mean subsidence velocity is an expected response to warming. However, this does not directly imply a weakening of the mean circulation as measured by the rate that mass circulates. In order to say something about potential changes to the mean circulation with warming, it is necessary to take into account any changes in the fractional areas covered by mean ascent and descent.

We define regions of ascent and descent at each level based on their daily mean vertical velocity. Mass balance requires that the mass fluxes of the ascending and descending regions are equal. This can be written as

$$\overline{M_{up}} = -\overline{M_{dn}} \equiv \overline{M}, \tag{5}$$

or as

$$\overline{w_{up}}\rho_{up}\alpha_{up} = -\overline{w_{dn}}\rho_{dn}\alpha_{dn}. \tag{6}$$

In these equations, the subscripts "up" and "dn" refer to regions of ascent ($\bar{w} > 0$) and descent ($\bar{w} < 0$), respectively. In 5, we take advantage of the fact that $\overline{M_{up}} = -\overline{M_{dn}}$ to define the symbol $\overline{M}$ (no subscript), which can be called the mass flux of the "overturning circulation." For our simulations of global RCE without rotation, we can take advantage of the weak horizontal temperature gradients and apply Equation 2 to

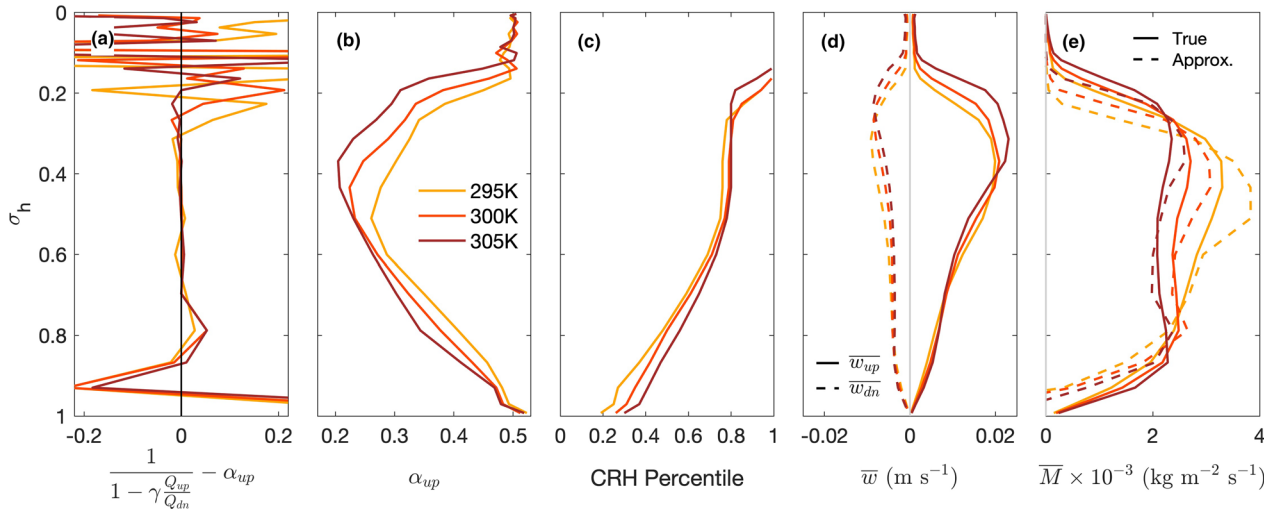

Figure 2. (a) The difference between the approximate fractional ascent area, α_{up}, given by Equation 7 and the true α_{up}. (b) α_{up}. (c) The column relative humidity (CRH) percentile that separates regions of mean ascent (right of the line) from regions of mean descent (left of the line). (d) The mean vertical velocity, $\bar{w}$, for the ascending (solid line) and descending (dashed line) regions. (e) The true (solid) and approximated, using Equation 9 (dashed) mass flux of the mean circulation, $\overline{M}$.

substitute for the vertical velocities in Equation 5 in terms of the area-averaged heating rates. Assuming that $\rho_{up} \approx \rho_{dn}$, and making the substitution $\alpha_{dn} = 1 - \alpha_{up}$, we find that

$$\alpha_{up} \approx \frac{1}{1 - \gamma \frac{\overline{Q_{up}}}{\overline{Q_{dn}}}}, \tag{7}$$

where we define

$$\gamma \equiv \frac{(\partial \bar{s}/\partial z)_{dn}}{(\partial \bar{s}/\partial z)_{up}}, \tag{8}$$

and $\overline{Q}$ is the mean total heating (i.e., $\overline{Q_R} + \overline{Q_c}$). Neglecting the effects of differences in the dry static stability between the ascending and descending regions (i.e., for $\gamma \approx 1$), Equation 7 says that the fractional area covered by mean ascent decreases as the ratio of mean total heating between the ascending and descending regions increases. The ratio $\overline{Q_{up}}/\overline{Q_{dn}}$ is always ≤ 0. In fact, we can use Equation 7 to show that for, $\gamma = 1$, the area-averaged heating rate (across both ascending and descending regions) is 0. When the mean (absolute) heating rates of the two regions are equal, $\overline{Q_{up}} = \overline{Q_{dn}}$ and 7 gives $\alpha_{up} = 0.5$. Larger heating rates in the ascending region, relative to the cooling rates in the descending region, imply stronger rising vertical velocities in the ascending region than sinking vertical velocities in the descending region (Equation 2). The descending region must therefore cover a larger fractional area than the ascending region. This is what we see in our simulations. Figure 2a shows the difference between α_{up} calculated using Equation 7 and the true α_{up}. Throughout the midtroposphere, roughly between levels $\sigma_h = 0.7$ and $\sigma_h = 0.3$, the approximate α_{up} given by Equation 7 is nearly equal to the true α_{up}, shown in Figure 2b. That is, between these levels, the error of the approximation is small. The approximation slightly overestimates α_{up} between $\sigma_h = 0.9$ and $\sigma_h = 0.7$ and is very poor in the boundary layer and stratosphere. At low levels, while some of the disagreement between the approximation and α_{up} may be due to differences in density between the humid ascending and dry descending regions, it is more likely driven by the weaker applicability of the WTG approximation at those levels.

Figure 2c shows the percentile of the column relative humidity (CRH; column precipitable water divided by the precipitable water of a saturated column with the same temperature profile) where these regions tend to be located. Regions of ascent in the upper troposphere have CRH values larger than about 0.75, while ascending air can occur in the lower troposphere even for CRH values less than 0.5.

Figure 2d shows the mean vertical velocity in the ascending and descending regions. Mean rising motions are stronger than sinking motions throughout most of the troposphere. Again, ignoring the small differences in static stability between the ascending and descending regions, Figure 2d together with Equation 2

implies that the heating in the ascending region is stronger than the cooling in the descending region. This is reflected in the values of α_{up}, which are less than 0.5 at almost all levels.

In addition to a weakening of the mean subsidence velocity, we find that the fractional area covered by the ascending region decreases with SST. This decrease is stronger in the upper troposphere, above $\sigma_h = 0.5$. At those same levels the fractional area covered by subsidence increases with SST. Figure 2e shows that the overturning mass flux (which is equal and opposite between the ascending and descending regions) weakens with warming throughout most of the troposphere (between about $\sigma_h = 0.9$ and $\sigma_h = 0.25$). This is consistent with previous work and reflects the fact that both the fractional area of the ascending region and the mean vertical velocity in the ascending region decrease with increasing SST.

Using our approximation for α_{up} with Equation 2, we can approximate the strength of the overturning circulation by

$$\overline{M} \approx \frac{\rho}{(\partial \bar{s}/\partial z)_{up}} \left(\frac{\overline{Q_{up}}\ \overline{Q_{dn}}}{\overline{Q_{dn}} - \overline{Q_{up}}} \right). \tag{9}$$

The approximate values are shown as the dashed line in Figure 2e. At most levels, the approximation accurately diagnoses the vertical profile of $\overline{M}$ and its decrease with SST, although there are some larger errors in the upper troposphere (between $\sigma_h = 0.6$ and $\sigma_h = 0.3$). Equation 9 directly shows how the strength of the mean circulation is inversely proportional to the dry static stability in the ascending region. For $\gamma \approx 1$, this means that the strength of the mean circulation is inversely proportional to the mean tropical dry static stability. Equation 9 shows that increases in $\overline{M}$ may be possible given larger fractional increases in the term, $\frac{\overline{Q_{up}}\ \overline{Q_{dn}}}{\overline{Q_{dn}} - \overline{Q_{up}}}$, than in dry static stability.

We can use Equation 9 to explore the magnitude of changes in $\overline{Q_{up}}$ and $\overline{Q_{dn}}$ required to strengthen $\overline{M}$. Figure 3a shows, for $\sigma_h = 0.51$, the percent change in $\overline{M}$ that results from prescribed fractional changes in the $\overline{Q_{up}}$ and $\overline{Q_{dn}}$ of the 295 K simulation, given the change in the dry static stability between the 295 and 300 K simulations. In the descending region, a positive change indicates an intensification of the cooling. We include lines showing the 0% change in heating. At their intersection, we see that between the 295 and 300 K simulations, $\overline{M}$ would weaken due to the increased dry static stability alone. The horizontal dashed line shows the simulated percent change of $\overline{Q_{dn}}$ between 295 and 300 K. Given the simulated strengthening of cooling in the descending region ($\approx +4\%$ between the 295 and 300 K simulations) at this level, we would begin to see an increase in the strength of the circulation for around a doubling of the heating in the ascending region.

Figure 3b shows the simulated percent change in $\overline{Q_{dn}}$ between the 295 and 300 K simulations (orange line) and between the 295 and 305 K simulations (brown line) at each model level. Figure 3c shows the simulated change in $\overline{Q_{up}}$ (solid lines) and the change in $\overline{Q_{up}}$ that would be required to get a strengthening of $\overline{M}$ at that level, given the simulated changes in $\overline{Q_{dn}}$ and dry static stability (dashed line). Throughout the midtroposphere (between $\sigma_h = 0.8$ and about $\sigma_h = 0.4$), the simulated increase in $\overline{Q_{up}}$ is smaller than the change in $\overline{Q_{up}}$ needed to strength the mean circulation. Between the 295 and 300 K simulations, and for σ_h in the range 0.95 to 0.8, we see the opposite: The increase in $\overline{Q_{up}}$ exceeds that needed to strengthen $\overline{M}$. This is consistent with the pattern of $\overline{M}$ change that is simulated by the numerical model (see the solid curves in Figure 2e).

In the quiescent descending region, midtropospheric changes in cooling with surface warming are dominated by small increases in radiative cooling. As the surface warms, the fractional rate of increase in radiative cooling is smaller than that of the dry static stability. Increases in the strength of the mean circulation would be possible only with very large and implausible increases in heating in the ascending region. This is another way of understanding why the overturning circulation weakens with warming.

We can use Equation 7 to gain insight into the physical processes involved with the decrease of α_{up} with increasing SST. Figure 4a shows γ and $-\overline{Q_{up}}/\overline{Q_{dn}}$. Throughout most of the troposphere ($\sigma = 0.8$ through $\sigma = 0.4$), $\gamma \approx 1$ and is not sensitive to the SST. From Figure 4a, we see that increases in $-\overline{Q_{up}}/\overline{Q_{dn}}$ are associated with the decrease in α_{up} with SST. Figure 4b shows $\overline{Q_{up}}$ and $\overline{Q_{dn}}$ for each SST. In the descending region, cooling intensifies as the SST increases, throughout most of the column. This is due to increased longwave emission to space from a warmer, wetter atmosphere (e.g., Pendergrass & Hartmann, 2014). With no change in $\overline{Q_{up}}$, the stronger radiative cooling rate in the descending region would lead to an *increase* in

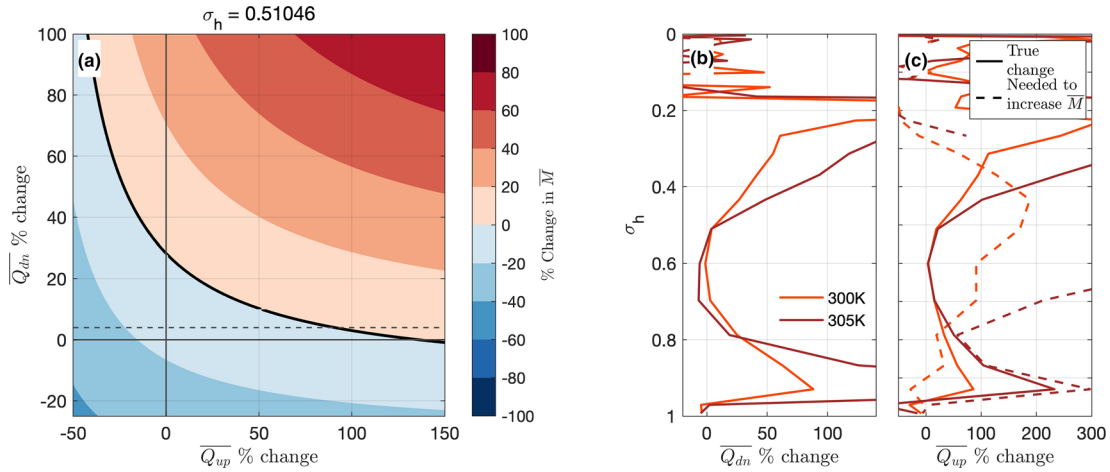

Figure 3. (a) At $\sigma_h = 0.51$, the percent change in the strength of the mean circulation, $\overline{M}$, that results from prescribed fractional changes in $\overline{Q_{up}}$ and $\overline{Q_{dn}}$ of the 295 K simulation, given the change in the dry static stability between the 295 and 300 K simulations. The dashed line shows the percent change in $\overline{Q_{dn}}$ between the 295 and 300 K simulations. (b) The simulated percent change in $\overline{Q_{dn}}$ between the 295 and 300 K simulations (orange) and between the 300 and 305 K simulations (brown). (c) The simulated percent change in $\overline{Q_{up}}$ (solid) and the percent change in $\overline{Q_{up}}$ needed to strengthen $\overline{M}$ (dashed).

α_{up}. But what we actually see is a decrease in α_{up}, because the mean heating rate in the ascending region is also intensifying, and at a faster rate than the cooling over the descending region (i.e., $-\overline{Q_{up}}/\overline{Q_{dn}}$ increases). This provides support for the suggestion of Schiro et al. (2019) that changes to convection in the ascending region are closely linked to changes in ascent area with warming.

Figure 4c shows the contributions to $\overline{Q_{up}}$ from both nonradiative processes ($\overline{Q_c}$) and radiation. The radiative portion is further subdivided into its longwave $\overline{Q_{Rl}}$ and shortwave $\overline{Q_{Rs}}$ parts. Longwave cooling intensifies in the ascending region (just as it does in the descending region), but there is very little change in shortwave heating of the ascending region. The main message of Figure 4c is that the increases in $\overline{Q_{up}}$ with SST in the ascending region are due to increases in nonradiative heating.

For a GCM grid cell, the mass flux of the mean circulation, $\overline{M}$, can be written as the sum of the net convective mass flux M_c and the "environmental" mass flux $\tilde{M}$ (Arakawa & Schubert, 1974):

$$\overline{M} = M_c + \tilde{M}. \tag{10}$$

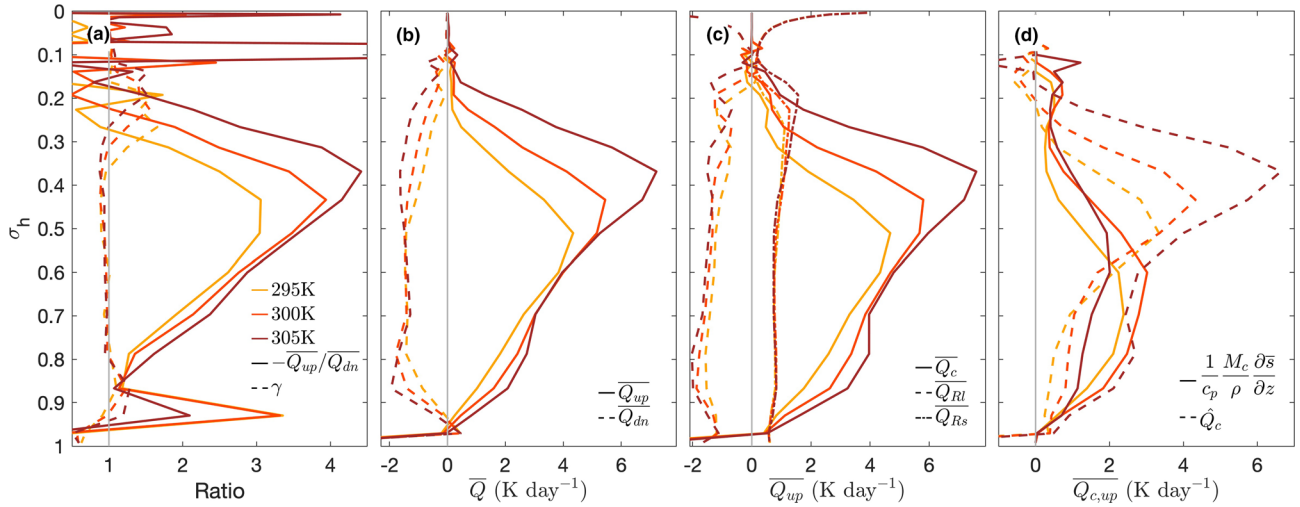

Figure 4. (a) Minus the ratio of total heating between the ascending and descending regions (solid) and γ from Equation 7. (b) Total heating for the ascending (solid) and descending (dashed) regions. (c) For the ascending region only, nonradiative (solid), longwave radiative (dashed), and shortwave radiative (dash-dotted) heating. (d) For the ascending region only, heating associated with the convective mass flux ($\frac{1}{c_p}\frac{M_c}{\rho}\frac{\partial \overline{s}}{\partial z}$; solid) and stratiform heating ($\widehat{Q_c}$; dashed).

The environmental mass flux is associated with weak vertical motion in the broad regions between the convective updrafts and downdrafts. It is typically but not always downward. Equation 10 shows that when convection is not active the mean mass flux is equal to the environmental mass flux; without convection, the domain is "all environment."

For averages over areas large enough so that the fractional area occupied by convective updrafts is $\ll 1$ (such as a GCM grid cell), $\overline{Q_c}$ may be written as

$$\overline{Q_c} = \frac{M_c}{\rho}\frac{\partial \bar{s}}{\partial z} + L\tilde{C} + \bar{D}(s_c - \bar{s}) + \overline{Q_{turb}}, \tag{11}$$

where $\frac{M_c}{\rho}\frac{\partial \bar{s}}{\partial z}$ is the warming due to the net convective mass flux, L is the latent heat of condensation and/or freezing, $\tilde{C}$ is the environmental condensation rate, $\bar{D}$ is the detrainment mass flux, and $\overline{Q_{turb}}$ is the dry static energy transport due to turbulence (Arakawa & Schubert, 1974). We can isolate the (nonradiative) cloud and turbulent heating apart from (i.e., not including) the contribution from $\frac{M_c}{\rho}\frac{\partial \bar{s}}{\partial z}$ using Equation 11 as

$$\widehat{Q_c} = \overline{Q_c} - \frac{M_c}{\rho}\frac{\partial \bar{s}}{\partial z}, \tag{12}$$

where we define

$$\widehat{Q_c} \equiv L\tilde{C} + \bar{D}(s_c - \bar{s}) + \overline{Q_{turb}}. \tag{13}$$

We use 12 to diagnose $\widehat{Q_c}$ from the model output. Equation 13 shows that contributions to $\widehat{Q_c}$ come from environmental (nonconvective) condensation $L\tilde{C}$, convective detrainment of dry static energy $D(s_c - \bar{s})$, and turbulent transport of dry static energy, but for simplicity we refer to $\widehat{Q_c}$ as the "stratiform heating." A large fraction of $\widehat{Q_c}$ comes from phase changes that occur outside of convective updrafts. Houze (1977) used radar data with other observations to show that such stratiform condensation is a major component of the heating in tropical convective systems. We expect $L\tilde{C} > 0$ where there is environmental rising motion in near-saturated environments (e.g., in stratiform anvil clouds), and $L\tilde{C} < 0$ where condensed water/ice is evaporating/melting as it interacts with an unsaturated portion of the environment.

Figure 4d shows the nonradiative heating, $\widehat{Q_{c,up}}$, in the ascending region. The solid curves show $\frac{M_c}{\rho}\frac{\partial \bar{s}}{\partial z}$ and the dashed curves show $\widehat{Q_c}$. The increase in $\widehat{Q_c}$ with SST is roughly monotonic, except between the 295 and 300 K simulations where a small decrease between $\sigma_h = 0.7$ and $\sigma_h = 0.55$ may be due to the deepening of the troposphere. Interestingly, below $\sigma = 0.4$ the change in $\frac{M_c}{\rho}\frac{\partial \bar{s}}{\partial z}$ with SST is not monotonic. For the 295 and 300 K simulations, heating associated with M_c is larger than $\widehat{Q_c}$ below $\sigma_h = 0.6$. This is reversed in the 305 K simulation, in which $\widehat{Q_c}$ larger than $\frac{M_c}{\rho}\frac{\partial \bar{s}}{\partial z}$ throughout the troposphere. Above $\sigma_h = 0.5$ for all simulations, and throughout the troposphere for the 305 K simulation, most of the increase in the total $\overline{Q_c}$ of ascending regions comes from an increase in $\widehat{Q_c}$ with SST. Between the 295 and 300 K simulations, the increase in $\frac{M_c}{\rho}\frac{\partial \bar{s}}{\partial z}$ roughly equals that of $\widehat{Q_c}$.

3.2. Stratiform Heating

What accounts for the large increase of $\widehat{Q_c}$ with warming in the ascending regions? In the upper troposphere, the increase is directly related to the decrease in the fractional area of the ascending region with warming. Through its contribution to the increase in $\overline{Q_{up}}$, it plays a role in determining the response of the mean circulation to warming. That is, increases in $\widehat{Q_c}$ in the ascending region with SST keep the mean circulation from weakening as much as it would given no change in heating in the ascending region. In places where $\tilde{M}$ is upward we can write environmental latent heating, $L\tilde{C}$, in terms of the advection of environmental moisture by $\tilde{M}$ as,

$$L\tilde{C} \approx -L\frac{\tilde{M}}{\rho}\frac{\partial \tilde{q}}{\partial z}, \quad (\tilde{M} > 0), \tag{14}$$

where $\tilde{q}$ is the water vapor mixing ratio of the environment. We can use Equation 14 to estimate the fraction of $\widehat{Q_c}$ due to environmental condensation. The dashed lines in Figure 5 are the heating from $-L\frac{\tilde{M}}{\rho}\frac{\partial \overline{Q}}{\partial z}$ in ascending regions only. We compute this term for grid cells where $\tilde{M}$ is upward and then multiply the

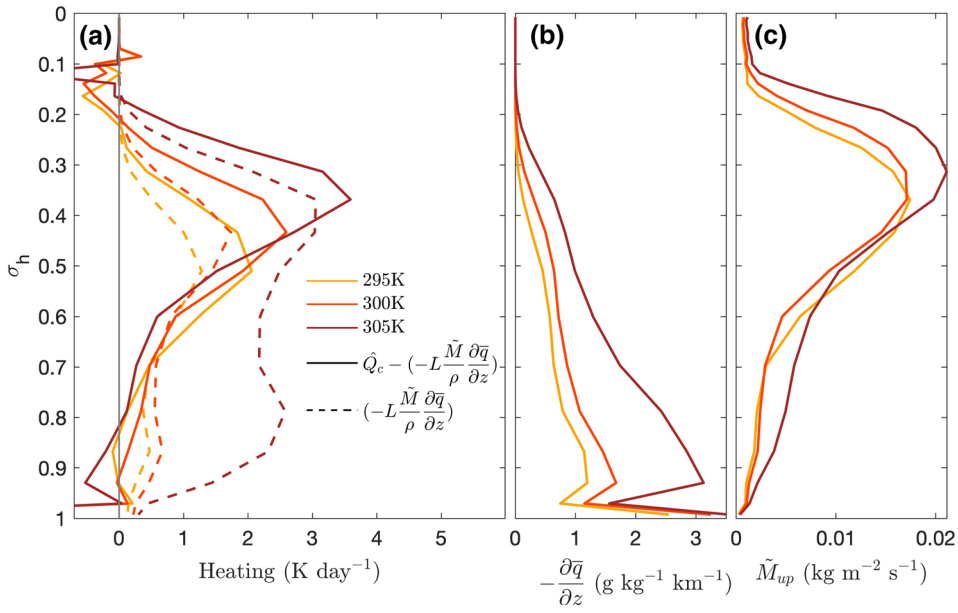

Figure 5. For ascending regions: (a) Contributions to $\widehat{Q_c}$ from environmental condensation, estimated as $-L\frac{\tilde{M}}{\rho}\frac{\partial\overline{Q}}{\partial z}$, and the remainder $\widehat{Q_c} - \left(-L\frac{\tilde{M}}{\rho}\frac{\partial\overline{Q}}{\partial z}\right)$. (b) Negative vertical water vapor mixing ratio gradient. (c) Mean upward $\tilde{M}$.

result by the fraction of the ascending region where $\tilde{M} > 0$. We use the grid cell mean water vapor mixing ratio, $\overline{Q}$, rather than the environmental $\tilde{q}$, and account for the ice phase using the temperature-dependent partitioning between the liquid and ice phases used in the model. The solid lines are the remainder when environmental condensation is subtracted from $\widehat{Q_c}$.

In ascending regions, heating due to environmental condensation increases with SST, particularly between the 300 and 305 K simulations. Figure 5b shows that most of this increase is from the stronger vertical moisture gradient, which increases following the increase in the slope of the saturation mixing ratio curve with temperature. Between the 300 and 305 K simulations, Figure 5c shows that below $\sigma_h = 0.6$ and above $\sigma_h = 0.4$ there is an additional contribution from a stronger upward $\tilde{M}$ (computed as the average $\tilde{M}$ where $\tilde{M} > 0$ multiplied by the fraction of the ascending region where $\tilde{M} > 0$).

We would like to point out that environmental air moving *upward* is interesting and contrary to how it is typically conceptualized. The environmental mass flux, as defined presently, is sensitive to our choice of the vertical velocity threshold we use to define convection, because we calculate $\tilde{M}$ using Equation 10. It is possible that we have underestimated the convective mass flux; if so, this would favor upward values of $\tilde{M}$. However, rising air in the environment is physically interpretable: Positive values of $\tilde{M}$ in the middle and upper troposphere favor the formation of stratiform anvil clouds, which are well understood to be important for the heating associated with mesoscale convective systems.

Equations 10 and 11 allow us to rewrite Equation 2 as

$$\frac{\tilde{M}}{\rho}\frac{\partial\overline{s}}{\partial z} = \overline{Q_R} + \widehat{Q_c}. \tag{15}$$

Writing WTG balance in terms of $\tilde{M}$, as in Equation 15, allows us to diagnose the relevant terms in the heating balance important for the environmental mass flux of a large area, regardless of whether or not the area contains convection (Arakawa & Schubert, 1974; Chikira, 2014). For grid cells containing active convection, Equation 15 says that the dry static energy advection by the environmental mass flux, $\frac{\tilde{M}}{\rho}\frac{\partial\overline{s}}{\partial z} = \frac{1}{\rho}(\overline{M} - M_c)\frac{\partial\overline{s}}{\partial z}$, balances the combination of stratiform heating and radiative cooling. For grid cells that do not contain active convection, $M_c = 0$, $\tilde{M} = \overline{M}$, $\widehat{Q_c}$ is typically negligible, and Equation 15 reduces to a balance between radiative cooling and advection of dry static energy by the mean vertical motion. Equation 15 shows us that the environmental mass flux of an area is upward when the net heating $\overline{Q_R} + \widehat{Q_c}$ is positive. Part of the heating

that the upward $\widetilde{M}$ balances is due to $\widetilde{M}$ being upward. That is, heating from environmental condensation associated with upward $\widetilde{M}$, in part balances the advective cooling due to the upward $\widetilde{M}$. This is a way to understand why $\widetilde{M}$ is upward.

In ascending regions, where an upward $\widetilde{M}$ contributes to $\widehat{Q_c}$, we can subtract the environmental condensation term, approximated using Equation 14, from $\widehat{Q_c}$ to roughly estimate the magnitude of heating from detrainment and turbulent fluxes. Figure 5a shows that this heating is large in the upper troposphere. Some of this it may be from a covariance between $\widetilde{M}$ and $\partial\widetilde{q}/\partial z$ on time scales faster than a day; these would be missed in our calculation of $L\widetilde{C}$ using daily mean values. The apparent importance of detrainment and turbulence in the heating budget in ascending regions requires further investigation. This is an important question because the increase of $\widehat{Q_c}$ with warming, which is largely contributed to by an increase in this residual heating term in the upper troposphere, is directly linked to the decrease of α_{up} with warming, and hence how the mean circulation responds to warming.

3.3. Response of the Convective Mass Flux to Warming

In our simulations of global RCE, the decrease of α_{up} with SST is directly related to fact that the net nonradiative heating in ascending regions intensifies faster than the radiative cooling in descending regions. In the upper troposphere, an increase in $\widehat{Q_c}$ explains most of the increase in the total $\overline{Q_c}$ in ascending regions, between the 300 and 305 K simulations. Much of the increase is due to the intensification of the vertical moisture gradient with warming. Between the 295 and 300 K simulations, there is an additional contribution to the increase in $\overline{Q_c}$ from $\frac{M_c}{\rho}\frac{\partial\bar{s}}{\partial z}$. Interestingly, this is not the case between the 300 and 305 K simulations, where $\frac{M_c}{\rho}\frac{\partial\bar{s}}{\partial z}$ in the ascending region *decreases* throughout the lower troposphere and midtroposphere. We are thus motivated to more closely investigate how the heating associated with the convective mass flux changes with increasing SST.

The nonmonotonic changes in $\frac{M_c}{\rho}\frac{\partial\bar{s}}{\partial z}$ in ascending regions are due to nonmonotonic changes in M_c with warming rather than changes in $\frac{\partial\bar{s}}{\partial z}$, which increases monotonically with SST. For the remainder of this section, we will thus focus on changes of the convective mass flux with SST.

We will extend this analysis to the entire domain, rather than just focusing on the ascending region alone, to get a more complete understanding of how M_c changes with SST. Figure 6a shows the vertical profiles of the global mean M_c. Consistent with previous work suggesting a decrease in M_c with warming (Held & Soden, 2006; Vecchi & Soden, 2007), we find that M_c weakens throughout the troposphere.

The decrease in the global mean M_c with SST is monotonic, with the largest decrease occurring between the 300 and 305 K simulations between about $\sigma_h = 0.9$ and $\sigma_h = 0.4$. When we separately consider ascending and descending regions, we find that the change of M_c with SST is not monotonic with SST and opposite between the regions. Figure 6e shows the total M_c in the ascending and descending regions. Below $\sigma_h = 0.35$, we see a very small increase (decrease) in M_c in ascending (descending) regions between the 295 and 300 K simulations. The change is opposite between the 300 and 305 K simulations, with M_c decreasing (increasing) in ascending (descending) regions. While the combination of the changes produces a monotonic decrease in the global mean M_c with SST, the region-specific patterns of change have unique effects on the heating budgets of the ascending and descending regions (and hence α_{up}). For example, the decrease of M_c in descending regions and increase in ascending regions that we observe between the 295 and 300 K simulations, neglecting how heating from other processes changes, increases the ratio $\overline{Q_{up}}/\overline{Q_{dn}}$, and hence contributes to a decrease in α_{up}. Conversely, the increase of M_c in descending regions and decrease in ascending regions that we observe between the 300 and 305 K simulations is related to the opposite change in α_{up}.

We subdivide M_c into contributions from weak, moderate, and intense convection following the definitions given in section 2.2. Figures 6b–6d show the global mean total M_c for convection in these intensity classifications and for each simulation. Convective mass fluxes from weak and moderate convection decrease with SST throughout the troposphere. Figure 6c shows that the large decrease in the global mean total M_c between $\sigma_h = 0.9$ and $\sigma_h = 0.6$ is mainly due to a decrease in M_c from moderate convection. Below $\sigma_h = 0.7$ there is very little change in M_c from intense convection between the 295 and 300 K simulations and a decrease between the 300 and 305 K simulations. Conversely, above $\sigma_h = 0.7$, we see an increase in M_c from intense convection between the 300 and 305 K simulation.

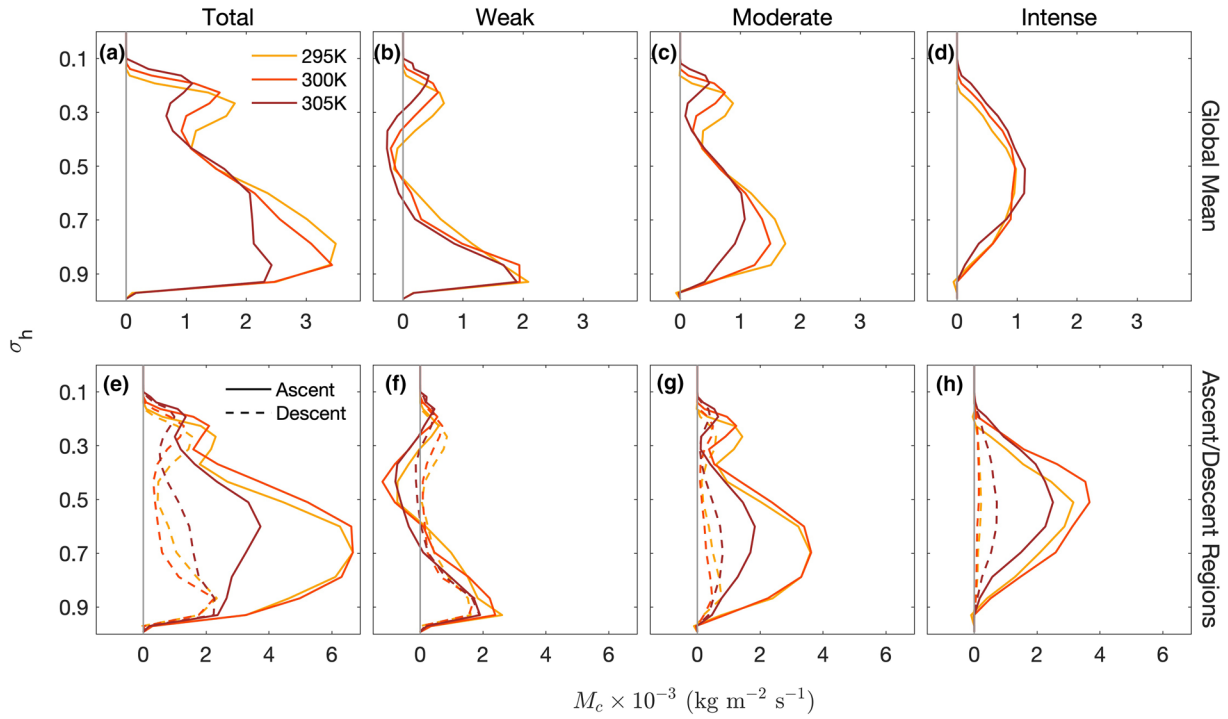

Figure 6. (a–d) Global mean profiles of simulated M_c for different intensity bins. (a) Total convective mass flux. (b) Convective mass flux from weak convection, (c) moderate convection, and (d) intense convection. (e–h) Mean convective mass flux for the ascending (solid) and descending (dashed) regions: (e) total, (f) weak convection, (g) moderate convection, and (h) intense convection.

Figures 6f–6h show M_c from weak, moderate, and intense convection in the ascending and descending regions. The magnitude of M_c from weak convection is comparable between the regions, except between $\sigma_h = 0.6$ and $\sigma_h = 0.3$ where M_c in the ascending region is negative and about 0 in the descending region. As in the pattern of change of the total M_c in ascending and descending regions with SST, the change of M_c from intense and moderate convection is nonmonotonic and opposite between the regions. We see from Figure 6g that the decrease of M_c from moderate convection below $\sigma_h = 0.5$ in the global mean profile comes from a decrease in M_c in descending regions between the 295 and 300 K simulations, with little change over the ascending region, and a large decrease between the 300 and 305 K simulations over the ascending region, while M_c in the descending region strengthens. For M_c from intense convection, the global mean increase that we observe above $\sigma_h = 0.65$ comes not from an intensification of M_c over ascending regions but from an intensification in *descending* regions (which is amplified in the global mean profile because of an increase in α_{dn}).

Changes to the mean convective mass flux can be due to changes in the frequency of convective updrafts, the vertical velocity of convective updrafts, and/or updraft fractional area.

In a warmer climate, updraft speeds are expected to intensify, with the largest increases occurring for the most intense updrafts (Singh & O'Gorman, 2015). This is related to a similar shift with warming in both modeled and observed precipitation (e.g., Chou et al., 2012; Del Genio et al., 2007; Fischer & Knutti, 2016, Lau et al., 2013; Pendergrass & Hartmann, 2014; Sun et al., 2007). Figures 7a and 7d show the log_{10} distribution of vertical velocities in ascending and descending regions, respectively. Frequencies are calculated as the average fraction of GCM grid cells with at least one CRM grid column containing an hourly vertical velocity that exceeds a threshold value. These frequencies thus include information about the number of GCM grid cells in the ascending/descending region containing an updraft at a certain speed (areal coverage) and the temporal frequency of the updraft speed. Strong vertical velocities are more common in the ascending than in the descending region.

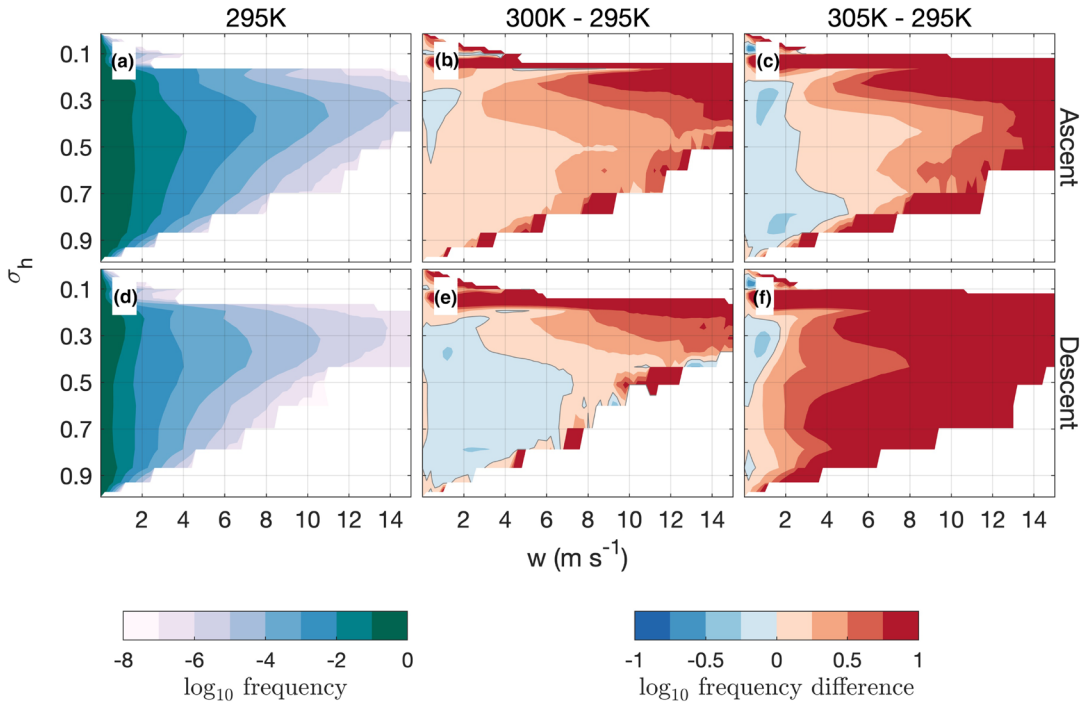

Figure 7. For the 295 K simulation, the frequency of hourly mean vertical velocities on the CRM grid exceeding threshold values for the (a) ascending and (d) descending regions. (b) Difference in the frequency between the 300 and 295 K simulations for the ascending region and (e) descending region. (c) Difference in the frequency between the 305 and 295 K simulations for the ascending region and (f) descending region.

Figures 7b and 7c show the differences in the frequency distributions of vertical velocities between the 295 K and warmer simulations in the ascending region. Note that the differences in Figures 7b, 7c, 7e, and 7f are also in log_{10} space and therefore should be interpreted as ratios rather than arithmetic differences. Changes between the distributions can be influenced by changes to the fraction of GCM grid cells within each region containing updrafts at a certain speed and/or by changes to the temporal frequency of those updrafts. Between the 295 and 300 K simulations, we see an increase in the frequency of all updraft speeds at all levels, except at speeds below 2 m s^{-1} between $\sigma_h = 0.5$ and $\sigma_h = 0.35$. This is consistent with the intensification of M_c that we observe in the ascending region between these two simulations. Between the 295 and 305 K simulation, we now see a decrease in the frequency of all updrafts (blue colors between threshold vertical velocities of 0 and about 2 m s^{-1}), with an intensification of the frequency of the strongest updrafts (> about 2 ms^{-1} above $\sigma_h = 0.7$ and > about 4 m s^{-1} between $\sigma_h = 0.9$ and $\sigma_h = 0.7$). Again, this is consistent with the weakening of M_c that we observe in ascending regions between these simulations.

Figures 7e and 7f show the differences in the frequency distributions of vertical velocities between the 295 K and warmer simulations in the descending region. Here we see a decrease in the frequency of all updrafts between the 295 K and warmer simulations, except between $\sigma_h = 0.8$ and $\sigma_h = 0.6$ between 295 and 305 K. The patterns of change, however, are quite different between Figures 7e and 7f. Between the 295 and 300 K simulations, updrafts decrease in frequency at almost all speeds, except in the upper troposphere for $w > 3$ m s^{-1}. Between the 295 and 305 K simulations, however, we see an increase in the frequency of all updrafts stronger than about 2 m s^{-1} throughout the column.

Generally, we observe an increase in the frequency of intense vertical velocities, which agrees with previous work showing that the vertical velocity distribution becomes more positively skewed with warming (Pendergrass & Gerber, 2016). This is directly related to an increase in the mean convective available potential energy (CAPE). Figure 8 shows the mean undilute CAPE for parcels lifted from the lowest model level as a function of CRH. The maximum CAPE shifts toward wetter columns in the warmer simulations. There is also an increase in the magnitude of the maximum CAPE by about 500 J kg^{-1} with each 5 K increase in SST.

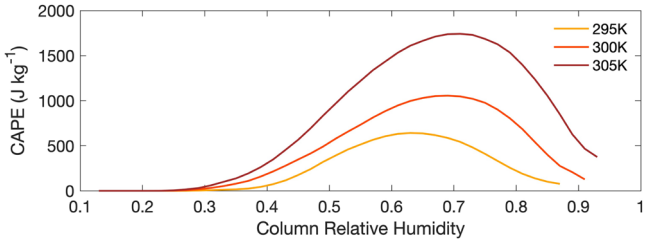

Figure 8. Simulated mean convective available potential energy (CAPE) for a parcel based in the lowest model level as a function of column relative humidity.

Figures 9a and 9d show the average updraft fractional area in ascending and descending regions for the 295 K simulation. This is calculated as the average fraction of the CRM grid with vertical velocities exceeding a threshold value, neglecting GCM grid cells that have no updrafts at or exceeding the threshold intensity. Above about 1 m s^{-1}, the fraction of the CRM domain within each GCM grid cell that is ascending is larger in the ascending than in the descending region. As expected, strong updrafts occupy a smaller fraction of the area in both regions.

Figures 9b and 9c show the differences in the updraft fractional area distributions between the 295 K and warmer simulations in the ascending region. The patterns of change are similar to those for the velocity distributions. Between the 295 and 300 K simulations, the fractional area occupied by updrafts generally increases throughout the column (except for large vertical velocities and at the upper levels). Between the 295 and 305 K simulations, weak updrafts become much (>10%) smaller while strong updrafts (>1 m s^{-1}) become larger.

Figures 9e and 9f show the differences in the updraft fractional area distributions between the 295 K and warmer simulations in the descending region. Changes between the 295 and 300 K simulations are small. Interestingly, between the 295 and 305 K simulations, we see a large increase in updraft fractional area for all intensities throughout most of the column.

In summary, despite a monotonic decrease in the global mean M_c, we find nonmonotonic changes when we subdivide by the ascending and descending regions. In general, convective updrafts become less common with increased SST, with increases in the size and frequency of the strongest updrafts. However, when looking at changes in just the ascending and descending regions, we find variations that are not consistent with SST and region. A particularly interesting result is the simultaneous decrease in M_c in ascending regions and increase in descending regions between the 295 and 305 K simulations. That is, the ascending and descending regions are becoming more similar to each other in the 305 K simulation.

3.4. Humidity Dependence

Up until this point, we have discussed changes to the circulation using averages of quantities taken over very large areas, that is, either the entire domain or the ascending/descending regions. In this section, we will discuss the variations to the mean circulation, convective mass flux, and heating terms with SST in more detail by looking at these terms in CRH space. In the real world, tropical temperature and pressure are close to uniform. Moisture and convective morphology, however, are not. Regions of active deep convection and mean ascent are generally located in the most humid parts of the tropics. Regions of mean descent are conversely located in drier regions. Analyzing changes to the circulation in humidity space thus allows us to assess regional changes. In our global RCE simulations, humid regions move around in space and time rather than being linked to geographically fixed SST patterns, the presence of land and topography, or rotation, as they are on Earth. Figure 10 shows the average daily distribution in percent of global area covered by various CRHs on the GCM grid. Values at the extremes of the distribution are rare but become more common in the warmer SST simulations. This is seen as a widening and flattening of the CRH distribution, with values drier than 0.5 and wetter than 0.8 both becoming more common with warming, at the expense of the moderate CRHs. An increase in the frequency of dry columns may be associated with an increased state of organization, which dries the atmosphere.

Figure 11a shows $\overline{M}$ for the 295 K simulation binned by CRH percentile. We bin by percentile here because of the shift in the distribution of CRH and in order to capture differences between the distributions while retaining all of the data. In this figure, the curve separating regions of descent and ascent slopes from drier

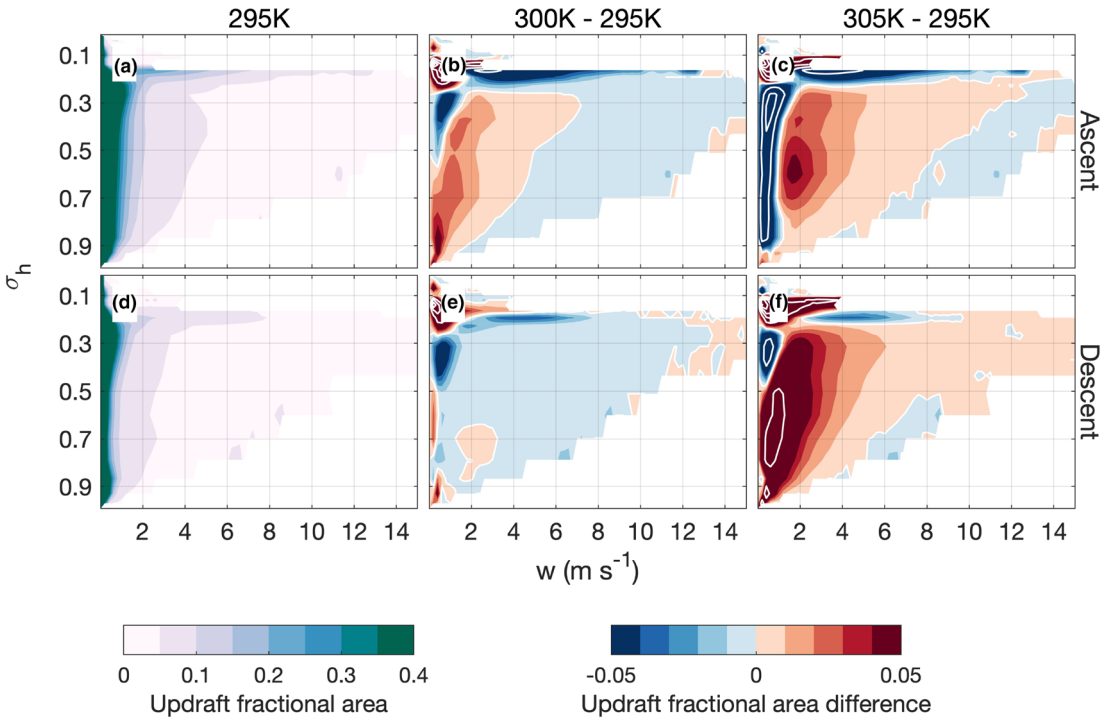

Figure 9. For the 295 K simulation, the average updraft fractional area, calculated as the average fraction of the CRM grid with vertical velocities exceeding threshold values for the (a) ascending and (d) descending regions. (b) Difference in the average updraft fractional area between the 300 and 295 K simulations for the ascending region and (e) descending region. (c) Difference in the average updraft fractional area between the 305 and 295 K simulations for the ascending region and (f) descending region. White contours in (b), (c), (e), and (f) are drawn every ±0.10 starting at 0.

columns at low levels to wetter columns at the upper levels. Figures 11b and 11c show the difference of $\overline{M}$ binned by CRH percentile between the 300 and 295 K simulations and between the 305 and 295 K simulations, respectively. As we showed in Figure 2e, $\overline{M}$ weakens with increasing SST between $\sigma_h = 0.8$ and $\sigma_h = 0.3$. Figures 11b and 11c show that the intensification of $\overline{M}$ at low levels is occurring for most values of the CRH.

The largest decreases in $\overline{M}$ below $\sigma_h = 0.3$ are in columns more humid than the 80th percentile of the CRH. Figures 11d–11f show $\overline{Q} = \overline{Q_c} + \overline{Q_R}$ binned by CRH for the 295 K simulation and its difference from the warmer simulations. Between $\sigma_h = 0.5$ and $\sigma_h = 0.3$, $\overline{Q}$ in this area is increasing with SST, with little change in $\overline{Q}$ below $\sigma_h = 0.5$. We conclude that the decreases in $\overline{M}$ that occur for columns more humid than the 80th percentile of CRH and between $\sigma_h = 0.8$ and $\sigma_h = 0.3$ are driven by increases in $\frac{\partial \bar{s}}{\partial z}$. In the part of the column where $\overline{Q}$ is intensifying but $\overline{M}$ is weakening, the increases in dry static stability are outpacing those of $\overline{Q}$.

In the previous section we showed that the global mean convective mass flux in our global RCE simulations decreases with increasing SST due to a general decrease in the frequency of weak and moderate updrafts. M_c associated with intense convection increases in the 305 K simulation mainly because of increases in the frequency and areal coverage of strong updrafts in descending regions. We now analyze changes in M_c and related quantities in CRH space to paint a more detailed picture of what is happening in our simulations.

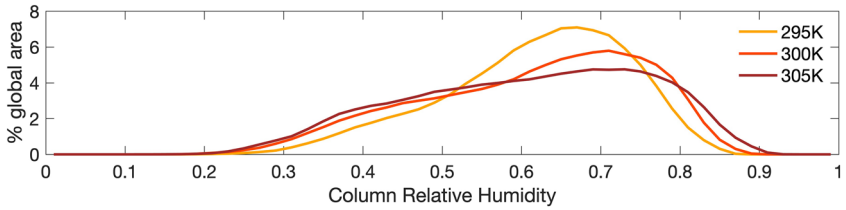

Figure 10. Frequency distribution, in average daily percent global area covered, of column relative humidities for bins 0.02 wide.

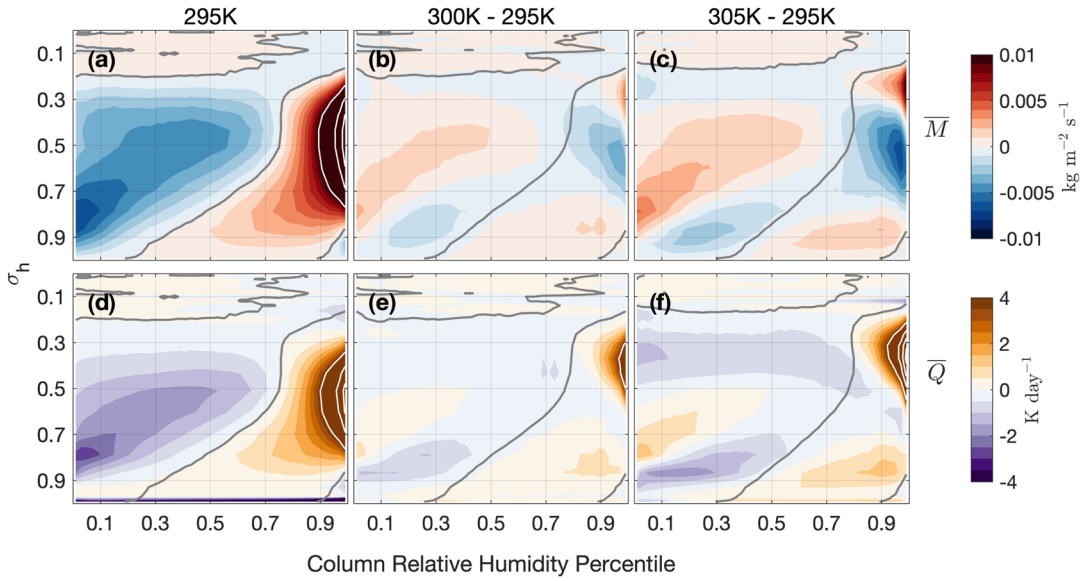

Figure 11. Mean mass flux, $\overline{M}$ (a–c), and total heating $\overline{Q}$ (d–f), binned by column relative humidity (CRH) percentile. (a) $\overline{M}$ for the 295 K simulation. (b) Difference of $\overline{M}$ between the 300 and 295 K simulations. (c) Difference of $\overline{M}$ between the 305 and 295 K simulations. (d–f) As in (a)–(c) but for $\overline{Q}$. White contours in (a) and (d) are drawn every 0.01 kg m^{-2} s^{-1} and 4 K day^{-1} respectively. Gray contour line in all panels are the zero contour of $\overline{M}$ binned by CRH percentile for the
(a, d) 295 K, (b, e) 300 K, and (c, f) 305 K simulations.

Figure 12a shows the total M_c binned by CRH percentile for the 295 K simulation. The black contour shows the CRH that separates regions of descent (to the left of the line) from regions of ascent (to the right of the line). M_c is generally much larger in the the ascending region than in the descending region, and the strongest convective mass fluxes are located in the wettest columns. For columns within the 30th to 70th CRH percentiles, M_c has two maxima. The lower tropospheric maximum is associated with shallow cumulus convection, while the upper-level maximum may be associated with weak convection in stratiform clouds (Houze 1977). Figures 12b and 12c are similar but for the 300 and 305 K simulations, respectively. A general weakening of M_c with warming is apparent. Figures 13a–13c show the same information that is presented in Figures 12a–12c, but Figures 12b and 12c now show the difference between the warmer simulations and the 295 K simulation. The largest changes are generally in the wettest columns, above the 90th percentile of the CRH.

Figures 12d–12l and 13d–13l show M_c for weak, moderate, and intense convection binned by CRH percentile for each simulation and the differences in intensity-specific M_c between the 295 K and warmer simulations. Weak convection is shallow. It is the main contributor to the total convective mass flux at low levels for the driest columns, and near the tropopause for columns between the 30th and 50th percentiles of CRH. There is a secondary peak in M_c from weak convection over the the wettest columns (>95th percentile). This may be large-scale saturated ascent, rather than weak cumulus convection. Moderate convection extends higher than weak convection and has its strongest mass fluxes in the wettest columns. The convective mass flux of intense convection is located higher in the troposphere because large values of vertical velocity are more common there (see Figure 7a). It is located in columns where CAPE is large but in wetter columns than where CAPE is largest (see Figure 8). This is because CAPE maximizes in columns with CRHs around 70%, where dry air entrainment can decelerate cumulus updrafts (e.g. Romps & Kuang, 2010).

In the previous section we showed that the total M_c decreases monotonically with SST, despite competing and nonmonotonic trends between the ascending and descending regions. Between the 295 and 300 K simulations, we find an intensification of M_c in ascending regions despite a weakening of the total M_c. This is mainly due to an increase of M_c from moderate and intense convection in ascending regions. Figures 13b, 13e, 13h, and 13k show that this intensification is occurring in the wettest columns (CRH > 90th percentile). The weakening of the global mean M_c between these two simulations is driven by a decrease of M_c from

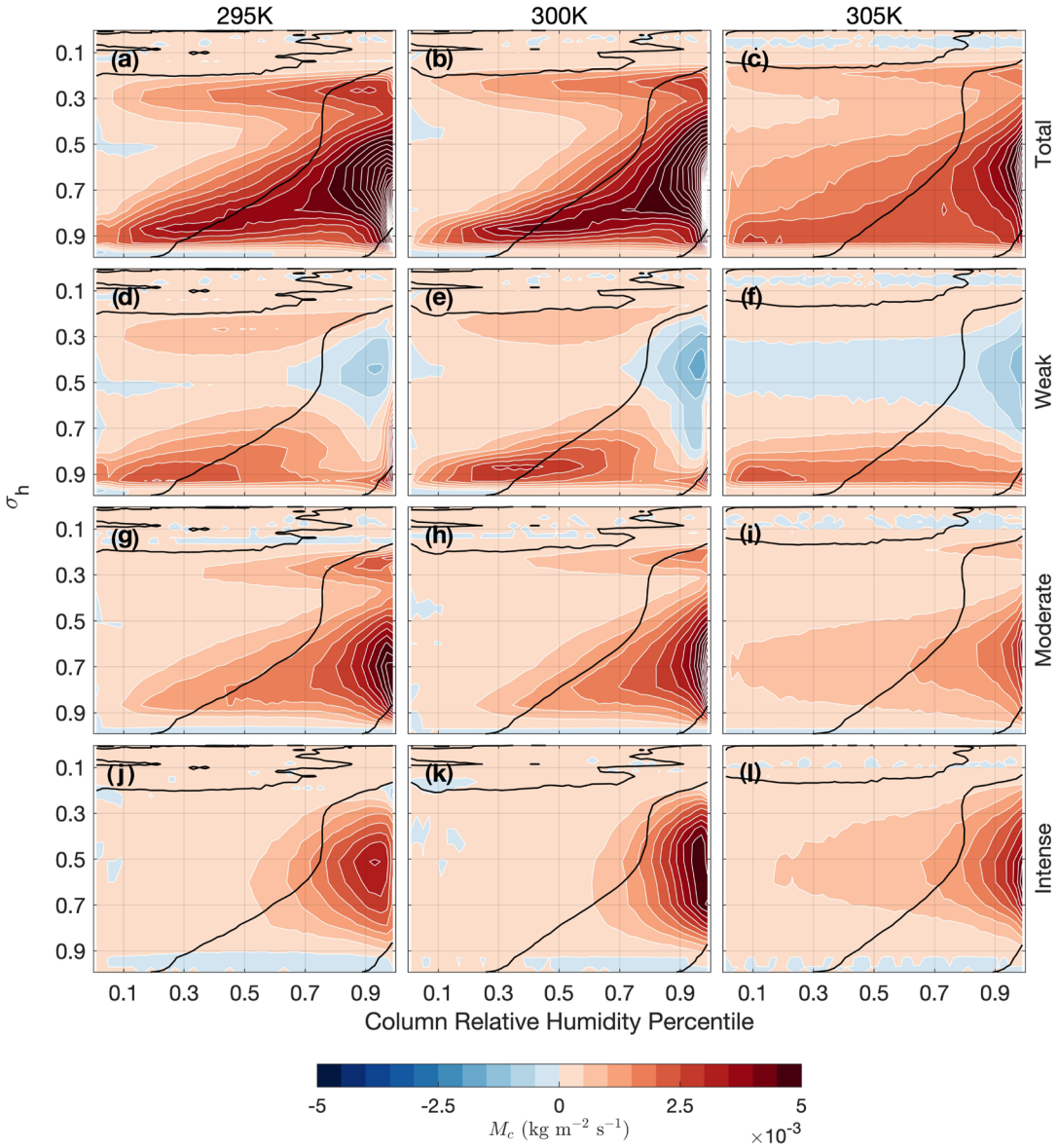

Figure 12. M_c binned by column relative humidity (CRH) percentile from (top row, a–c) all convection, (second row, d–f) weak convection, (third row, g–i) moderate convection, and (bottom row, j–l) intense convection. The left column (a, d, g, and j) shows values for the 295 K simulation, the center column (b, e, h, and k) shows values for the 300 K simulation, and the right column (c, f, i, and l) 305 K simulation. Black contour line in each panel is the zero contour line of the mean mass flux, $\overline{M}$, binned by CRH for the corresponding simulation.

convection of all intensities in the descending region, and is amplified by the increase in α_{dn}. Figures 13b, 13e, and 13h show that this weakening is spread across the descending region.

Between the 295 and 305 K simulations, there is a large decrease in M_c, primarily from a weakening of M_c from moderate convection in the ascending region (Figures 6g and 13i). This is despite an intensification of M_c from intense convection in the descending region. Looking at Figures 6h, 12l, and 13l, this increase in M_c in the descending region is small, and occurs for columns wetter than the 20th CRH percentile.

Neelin et al. (2003) and Chou and Neelin (2004) discuss mechanisms responsible for increases in precipitation at the centers of convective areas with simultaneous decreases at their edges. For the wettest regions, there is sufficient moisture to trigger deep convection. In warmer climates, more precipitation is produced in these regions because the air contains more water vapor. At the edges of the precipitation centers, precipitation is inhibited by dry air input resulting from stronger low level moisture gradients. We see this pattern

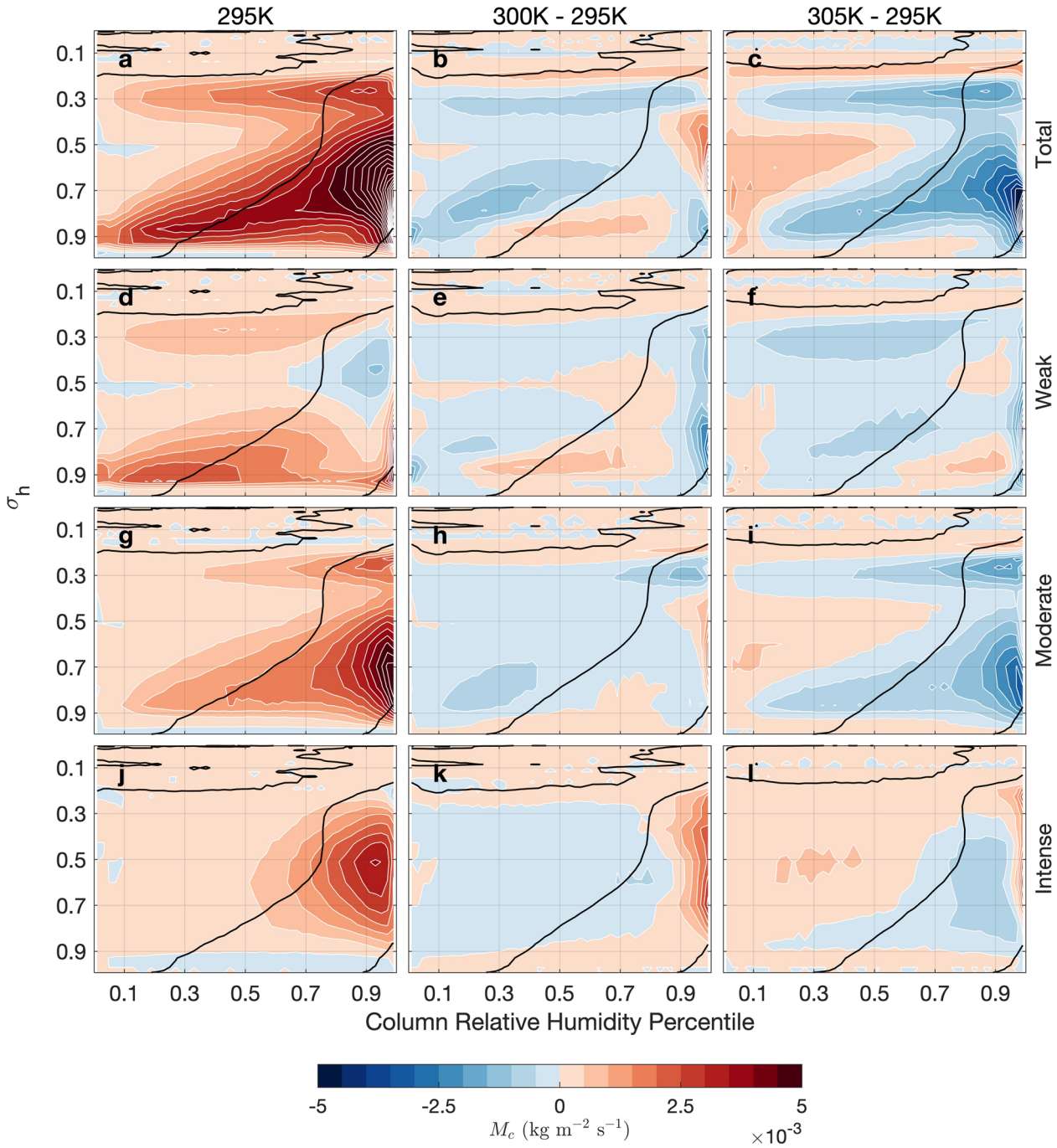

Figure 13. As in Figure 12 but the center and right columns now show the difference between the 300 and 295 K simulations (center column) and 305 and 295 K simulation (right column). Black contour line in each panel is the zero contour line of the mean mass flux, $\overline{M}$, binned by CRH for the (left column) 295 K, (center column) 300 K, and (right column) 305 K simulations.

of change in M_c, which is closely related to precipitation, in some of the differences between our simulations. Figures 13h, 13k, and 13l, which show the change in M_c between the 295 and 300 K simulations for the moderate and intense convection categories and between the 300 and 305 K simulations for the intense category, each have a pattern of intensifying convective mass fluxes in the wettest columns and a decrease at the margins. This pattern is most evident in Figure 13l. However, we do not observe this pattern in the difference of the overall M_c between the simulations (Figures 13b and 13c) and observe the reverse pattern for the change in M_c associated with weak convection (Figures 13e and 13f).

4. Discussion and Conclusions

The warming-induced weakening of the sinking in clear-sky regions can be understood by considering the tropical clear-sky energy balance. The atmosphere is continuously losing energy radiatively, and this energy sink is balanced by adiabatic descent and warming. For a given radiative cooling rate, the strength of the sinking motion is dictated by the mean tropical static stability profile, which is nearly constant throughout the real-world tropics due to the inability of the tropical atmosphere to support strong pressure gradients. The tropical static stability profile roughly follows a moist adiabat and will likely become more stable with surface warming in addition to becoming more stable in direct response to increased CO_2 (Merlis, 2015). Increased static stability makes sinking motions in clear-sky regions more efficient, so that for a given amount of radiative cooling slower subsidence is required to maintain energy balance.

This argument has been used to explain why the tropical circulation appears to weaken with warming. However, the rate that mass circulates through the mean flow also depends on the fractional area covered by the ascending and descending regions and the mean vertical velocity in the ascending regions.

We have used the WTG approximation, which is globally applicable in our idealized numerical simulations, to develop a simple diagnostic that links the fractional area covered by the ascending region (α_{up}) to the strength of the mean circulation. We show that it is a good approximation in simulations of global RCE using a model with SP convection. We use it to demonstrate how large increases in nonradiative heating in the ascending region are associated with the decrease in α_{up} with increasing SST.

We find that the increase in heating in the ascending region, $\overline{Q}_{up}$, is primarily due to an increase in what we have euphemistically called "stratiform heating," which includes heating due to environmental (nonconvective) condensation, detrainment, and turbulence. Most of this increase in the lower troposphere, and about half in the upper troposphere, can be explained by increases in the vertical moisture gradient with warming, which make latent heating via environmental condensation more efficient for a constant environmental mass flux in the spaces between the convective updrafts and downdrafts. An investigation of the changes to stratiform heating, and the relationship (if any) between stratiform heating and the heating associated with the convective mass flux, would be an interesting subject for future work.

Byrne and Schneider (2016a) recently developed a theory aimed at explaining the width of the Intertropical Convergence Zone (ITCZ) using an energetics framework. Byrne and Schneider (2016b) use this theory to analyze the observed and modeled contraction of the ITCZ with warming and determine that it is primarily the result of increased atmospheric moisture, which steepens the meridional moist static energy gradient and enhances ITCZ cooling through advective and eddy heat transfer. While we similarly find that increased atmospheric moisture is related to the contraction of the ascending area, our analysis shows that it is associated with increased heating in the ascending area. There are important differences between the framework proposed by Byrne and Schneider (2016a) and that outlined here. Our simple approximation for the fractional area of the ascending region is made possible by assuming WTGs, which allows us to neglect horizontal energy transport entirely. This is a good assumption for the tropics and for our global RCE simulations. On Earth, the Hadley circulation extends into the subtropics where stronger horizontal temperature gradients and rotation give rise to larger horizontal heat transports. Additionally, our framework applies to the total ascending area, rather than the area of the zonal mean tropical circulation. Nevertheless, our framework may useful for understanding warming-induced changes in the zonally asymmetric Walker circulation.

Using our diagnostic for α_{up}, we obtained an expression for the strength of the mean overturning circulation, $\overline{M}$. It is inversely proportional to the mean tropical dry static stability and proportional to the magnitude of the product of the mean heating rates over the ascending and descending regions. Increases in $\overline{M}$ with surface warming are possible given sufficient intensification of the heating in ascending regions and/or cooling in descending regions. The rate of increase in atmospheric radiative cooling with warming is small, however. We have shown that implausibly large increases in heating in the ascending regions would be needed to strengthen $\overline{M}$, given the rate that dry static stability strengthens with warming. This is why the strength of the mean circulation decreases with warming.

An important question is whether the framework that we have proposed for relating ascending area and the strength of the mean circulation to regional heating rates is too simple to be used to understand the real world. Popp and Bony (2019) noticed a relationship between the degree to which ITCZ convection is zonally

clustered and the strength and width of the ITCZ's circulation. They attribute the observed and modeled link between increased clustering and a weakening/widening of the Hadley circulation to decreases in the net heating of the ITCZ, which is in part due to increased radiative cooling from a larger equatorial nonconvective region. Their results suggest that the framework we have proposed may be useful for understanding observed variability in the tropical circulation. Other studies have attributed model spread in the simulation of ITCZ width to differences in the modeled response of clouds and radiation to warming (Su et al., 2019), much of which appears to be related to diversity in convective parameterizations (Schiro et al., 2019). Our results emphasize the importance of the net heating in the ascending, convective region for the tropical ascent area. We pose that a better understanding of how nonradiative heating over ascending regions responds to warming will help build confidence in future projections of tropical ascent area change.

We have also used our simulations of global RCE with SP convection to investigate changes to the convective mass flux, M_c, with warming. Consistent with Held and Soden (2006), we find decreases in M_c with increased SST. Generally, these decreases are due to less frequent convection, despite intensification of the strongest updraft speeds. Our use of a SP model with an Earth-like domain size makes this result particularly relevant to the real world. Previous work has investigated changes to M_c using simulations with parameterized convection (e.g., Vecchi & Soden, 2007).

When we investigate the warming-induced changes of M_c in more detail, we find that the largest changes tend to be located in the wettest columns (CRH percentile > 0.9), where M_c is already large. However, the fractional area covered by these columns is very small (see Figure 10). The change in M_c in the much broader dry descending region, despite its very weak magnitude, plays an important role in explaining why the global mean total M_c decreases monotonically with warming. These changes are reinforced by the increase in α_{dn} with SST. For reasons we have not determined, the change in M_c in the ascending and descending regions is nonmonotonic and opposite between the regions.

A limitation of our study is the simple bulk microphysics scheme employed by the model. Previous work has shown that in simulations of RCE, single-moment microphysics parameterizations underestimate low clouds when compared to two-moment schemes, which produce more realistic cloud fraction profiles (Igel et al., 2015). Simulated tropical ascent area has been demonstrated to be sensitive to cloud physics parameters (Schiro et al., 2019). Given the importance of clouds in the atmosphere's radiative heating budget, our results may be sensitive to the microphysics parameterization. The sensitivity of our results to the microphysics parameterization is left for future work.

Data Availability Statement

The data used in this study are available from the Mountain Scholar institutional repository managed by Colorado State University. It can be accessed online (https://hdl.handle.net/10217/199724).

Acknowledgments
We thank Prof. Elizabeth Barnes for helpful discussions. Funding support for this project comes from the National Oceanographic and Atmospheric Administration under Grant NA19OAR4590155 to Colorado State University. The simulations were performed using computational support from the National Center for Atmospheric Research (Cheyenne; doi: 10.5065/D6RX99HX).

References

Allen, M. R., & Ingram, W. J. (2002). Constraints on future changes in climate and the hydrologic cycle. *Nature*, *419*(6903), 228.

Arakawa, A., & Schubert, W. H. (1974). Interaction of a cumulus cloud ensemble with the large-scale environment, Part I. *Journal of the Atmospheric Sciences*, *31*(3), 674–701.

Betts, A. K. (1998). Climate-convection feedbacks: Some further issues. *Climatic Change; Dordrecht*, *39*(39), 35–38. https://doi.org/10.1023/A:1005323805826

Betts, A. K., & Ridgway, W. (1989). Climatic equilibrium of the atmospheric convective boundary layer over a tropical ocean. *Journal of the Atmospheric Sciences*, *46*(17), 2621–2641. https://doi.org/10.1175/1520-0469(1989)046<2621:CEOTAC>2.0.CO;2

Bui, H. X., & Maloney, E. D. (2018). Changes in Madden-Julian oscillation precipitation and wind variance under global warming. *Geophysical Research Letters*. *45*, 7148–7155. https://doi.org/10.1029/2018GL078504

Bui, H. X., & Maloney, E. D. (2019). Transient response of MJO precipitation and circulation to greenhouse gas forcing. *Geophysical Research Letters*, *7*, 847. https://doi.org/10.1029/2019GL085328

Byrne, M. P., Pendergrass, A. G., Rapp, A. D., & Wodzicki, K. R. (2018). Response of the Intertropical Convergence Zone to climate change: Location, width, and strength. *Current Climate Change Report*, *4*(4), 355–370.

Byrne, M. P., & Schneider, T. (2016a). Energetic constraints on the width of the intertropical convergence zone. *Journal of Climate*, *29*(13), 4709–4721. https://doi.org/10.1007/s40641-018-0110-5

Byrne, M. P., & Schneider, T. (2016b). Narrowing of the ITCZ in a warming climate: Physical mechanisms: Narrowing ITCZ: Physical mechanisms. *Geophysical Research Letters*, *43*, 11,350–11,357. https://doi.org/10.1002/2016GL070396

Charney, J. G. (1963). A note on large-scale motions in the tropics. *Journal of the Atmospheric Sciences*, *20*(6), 607–609.

Chikira, M. (2014). Eastward-propagating intraseasonal oscillation represented by Chikira–Sugiyama cumulus parameterization. Part II: Understanding moisture variation under weak temperature gradient balance. *Journal of Atmospheric Sciences*, *71*(2), 615–639. https://doi.org/10.1175/JAS-D-13-038.1

Chou, C., & Chen, C.-A. (2010). Depth of convection and the weakening of tropical circulation in global warming. *Journal of Climate*, *23*(11), 3019–3030. https://doi.org/10.1175/2010JCLI3383.1

Chou, C., Chen, C.-A., Tan, P.-H., & Chen, K. T. (2012). Mechanisms for global warming impacts on precipitation frequency and intensity. *Journal of Climate*, *25*(9), 3291–3306. https://doi.org/10.1175/JCLI-D-11-00239.1

Chou, C., & Neelin, J. D. (2004). Mechanisms of global warming impacts on regional tropical precipitation. *Journal of Climate*, *17*(13), 2688–2701. https://doi.org/10.1175/1520-0442(2004)017<2688:MOGWIO>2.0.CO;2

Del Genio, A. D., Yao, M.-S., & Jonas, J. (2007). Will moist convection be stronger in a warmer climate?: Convection strength in a warmer climate. *Geophysical Research Letters*, *34*, 1086. https://doi.org/10.1029/2007GL030525

Fischer, E. M., & Knutti, R. (2016). Observed heavy precipitation increase confirms theory and early models. *Nature Climate Change*, *6*(11), 986–991. https://doi.org/10.1038/nclimate3110

Grabowski, W. W. (2001). Coupling cloud processes with the large-scale dynamics using the cloud-resolving convection parameterization (CRCP). *Journal of Atmospheric Sciences*, *58*(9), 978–997. https://doi.org/10.1175/1520-0469(2001)058<0978:CCPWTL>2.0.CO;2

Held, I. M., & Soden, B. J. (2006). Robust responses of the hydrological cycle to global warming. *Journal of Climate*, *19*(21), 5686–5699. https://doi.org/10.1175/JCLI3990.1

Houze, R. A (1977). Structure and dynamics of a tropical squall–line system. *Monthly Weather Review*, *105*(12), 1540–1567.

Hu, Y., & Fu, Q. (2007). Observed poleward expansion of the Hadley circulation since 1979. *Atmospheric Chemistry and Physics.7*(19), 5229–5236

Igel, A. L., Igel, M. R., & van den Heever, S. C. (2015). Make it a double? Sobering results from simulations using single-moment microphysics schemes. *Journal of Atmospheric Sciences*, *72*(2), 910–925. https://doi.org/10.1175/JAS-D-14-0107.1

Khairoutdinov, M., & Randall, D. A. (2001). A cloud resolving model as a cloud parameterization in the NCAR community climate system model: Preliminary results. *Geophysical Research Letters*, *28*(18), 3617–3620. https://doi.org/10.1029/2001GL013552

Khairoutdinov, M., & Randall, D. A. (2003). Cloud resolving modeling of the ARM summer 1997 IOP: Model formulation, results, uncertainties, and sensitivities. *Journal of Atmospheric Sciences*, *60*(4), 607–625. https://doi.org/10.1175/1520-0469(2003)060<0607:CRMOTA>2.0.CO;2

Khairoutdinov, M., Randall, D., & DeMott, C. (2005). Simulations of the atmospheric general circulation using a cloud-resolving model as a superparameterization of physical processes. *Journal of Atmospheric Sciences*, *62*(7), 2136–2154. https://doi.org/10.1175/JAS3453.1

Knutson, T. R., & Manabe, S. (1995). Time-mean response over the tropical pacific to increased CO_2 in a coupled Ocean-Atmosphere model. *Journal Climate*, *8*(9), 2181–2199. https://doi.org/10.1175/1520-0442(1995)008<2181:TMROTT>2.0.CO;2

Kooperman, G. J., Pritchard, M. S., Burt, M. A., Branson, M. D., & Randall, D. A. (2016). Impacts of cloud superparameterization on projected daily rainfall intensity climate changes in multiple versions of the community earth system model. *Journal of Advances in Modeling Earth Systems*, *8*, 1727–1750. https://doi.org/10.1002/2016MS000715

Lau, W. K. M., & Kim, K.-M. (2015). Robust Hadley circulation changes and increasing global dryness due to CO_2 warming from CMIP5 model projections. *Proceedings of the National Academy of Science U. S. A.*, *112*(12), 3630–3635. https://doi.org/10.1073/pnas.1418682112

Lau, W. K.-M., Wu, H.-T., & Kim, K.-M. (2013). A canonical response of precipitation characteristics to global warming from CMIP5 models: Precipitation and global warming. *Geophysical Research Letters*, *40*, 3163–3169. https://doi.org/10.1002/grl.50420

Lu, J., Vecchi, G. A., & Reichler, T. (2007). Expansion of the Hadley cell under global warming. *Geophysical Research Letters*, *34*, 35. https://doi.org/10.1029/2006GL028443

Maher, P., Vallis, G. K., Sherwood, S. C., Webb, M. J., & Sansom, P. G. (2018). The impact of parameterized convection on climatological precipitation in atmospheric global climate models. *Geophysical Research Letters*, *45*, 3728–3736. https://doi.org/10.1002/2017GL076826

Merlis, T. M. (2015). Direct weakening of tropical circulations from masked CO_2 radiative forcing. *Proceedings of the National Academy of Science U. S. A.*, *112*(43), 13,167–13,171. https://doi.org/10.1073/pnas.1508268112

Neelin, J. D., Chou, C., & Su, H. (2003). Tropical drought regions in global warming and El Niño teleconnections. *Geophysical Research Letters*, *30*(24) 2275. https://doi.org/10.1029/2003GL018625

Pendergrass, A. G., & Gerber, E. P. (2016). The rain is askew: Two idealized models relating vertical velocity and precipitation distributions in a warming world. *Journal of Climate*, *29*(18), 6445–6462. https://doi.org/10.1175/JCLI-D-16-0097.1

Pendergrass, A. G., & Hartmann, D. L. (2014). The atmospheric energy constraint on global-mean precipitation change. *Journal of Climate*, *27*(2), 757–768. https://doi.org/10.1175/JCLI-D-13-00163.1

Popp, M., & Bony, S. (2019). Stronger zonal convective clustering associated with a wider tropical rain belt. *Nature Communications*, *10*(1), 4261. https://doi.org/10.1038/s41467-019-12167-9

Randall, D., DeMott, C., Stan, C., Khairoutdinov, M., Benedict, J., McCrary, R., et al. (2016). Simulations of the tropical general circulation with a multiscale global model. *Meteorological Magazine*, *56*, 15.1–15.15. https://doi.org/10.1175/AMSMONOGRAPHS-D-15-0016.1

Randall, D., Khairoutdinov, M., Arakawa, A., & Grabowski, W. (2003). Breaking the cloud parameterization deadlock. *Bulletin of the American Mathematical Society*, *84*(11), 1547–1564. https://doi.org/10.1175/BAMS-84-11-1547

Riehl, H., & Malkus, J. (1958). On the heat balance of the equatorial trough zone. *geophysica*, *6*, 3–4. Helsinki.

Romps, D. M., & Kuang, Z. (2010). Do undiluted convective plumes exist in the upper tropical troposphere? *Journal of Atmospheric Sciences*, *67*(2), 468–484. https://doi.org/10.1175/2009JAS3184.1

Schiro, K. A., Su, H., Wang, Y., Langenbrunner, B., Jiang, J. H., & Neelin, J. D. (2019). Relationships between tropical ascent and high cloud fraction changes with warming revealed by perturbation physics experiments in CAM5. *Geophysical Research Letters*, *46*, 10,112–10,121. https://doi.org/10.1029/2019GL083026

Schneider, T., O'Gorman, P. A., & Levine, X. J. (2010). Water vapor and the dynamics of climate changes. *Reviews of Geophysics*, *48*, D22104. https://doi.org/10.1029/2009RG000302

Seager, R., Naik, N., & Vecchi, G. A. (2010). Thermodynamic and dynamic mechanisms for large-scale changes in the hydrological cycle in response to global warming. *Journal of Climate*, *23*(17), 4651–4668. https://doi.org/10.1175/2010JCLI3655.1

Singh, M. S., & O'Gorman, P. A. (2015). Increases in moist-convective updraught velocities with warming in radiative-convective equilibrium: Increases in updraught velocities with warming. *Quarterly Journal of the Royal Meteorological Society*, *141*(692), 2828–2838. https://doi.org/10.1002/qj.2567

Sobel, A. H., & Bretherton, C. S. (2000). Modeling tropical precipitation in a single column. *Journal of Climate*, *13*(24), 4378–4392. https://doi.org/10.1175/1520-0442(2000)013<4378:MTPIAS>2.0.CO;2

Sobel, A. H., Nilsson, J., & Polvani, L. M. (2001). The weak temperature gradient approximation and balanced tropical moisture waves. *Journal of Atmospheric Sciences*, *58*(23), 3650–3665. https://doi.org/10.1175/1520-0469(2001)058<3650:TWTGAA>2.0.CO;2

Stevens, B., Satoh, M., Auger, L., Biercamp, J., Bretherton, C. S., Chen, X., et al. (2019). DYAMOND: The DYnamics of the Atmospheric general circulation Modeled On Non-hydrostatic Domains. *Progress in Earth and Planetary Science*, *6*(1), 61.

Su, H., Jiang, J. H., Neelin, J. D., Shen, T. J., Zhai, C., Yue, Q., et al. (2017). Tightening of tropical ascent and high clouds key to precipitation change in a warmer climate. *Nature Communications*, *8*, 15,771. https://doi.org/10.1038/ncomms15771

Su, H., Zhai, C., Jiang, J. H., Wu, L., Neelin, J. D., & Yung, Y. L. (2019). A dichotomy between model responses of tropical ascent and descent to surface warming. *npj Climate and Atmospheric Science*, *2*(1), 8. https://doi.org/10.1038/s41612-019-0066-8

Sun, Y., Solomon, S., Dai, A., & Portmann, R. W. (2007). How often will it rain? *Journal of Climate*, *20*(19), 4801–4818. https://doi.org/10.1175/JCLI4263.1

Vecchi, G. A., & Soden, B. J. (2007). Global warming and the weakening of the tropical circulation. *Journal of Climate*, *20*(17), 4316–4340. https://doi.org/10.1175/JCLI4258.1

Wing, A. A., Reed, K. A., Satoh, M., Stevens, B., Bony, S., & Ohno, T. (2018). Radiative–convective equilibrium model intercomparison project. *Geoscientific Model Development*, *11*(2), 793–813. https://doi.org/10.5194/gmd-11-793-2018

Wodzicki, K. R., & Rapp, A. D. (2016). Long-term characterization of the Pacific ITCZ using TRMM, GPCP, and ERA-Interim: Pacific ITCZ characterization. *Journal of Geophysical Research D: Atmospheres*, *121*, 3153–3170. https://doi.org/10.1002/2015JD024458

Wolding, B. O., Maloney, E. D., Henderson, S., & Branson, M. (2017). Climate change and the Madden-Julian oscillation: A vertically resolved weak temperature gradient analysis: Climate change and the MJO. *Journal of Advances in Modeling Earth Systems*, *9*, 307–331. https://doi.org/10.1002/2016MS000843